

Anomalous low-temperature dopant diffusivity and defect structure in Sb- and Sb/B-implanted annealed silicon samples

A. Armigliato

Consiglio Nazionale delle Ricerche, Istituto di Chimica e Tecnologia dei Materiali e Componenti per l'Elettronica (LAMEL), via P. Gobetti 101, 40129 Bologna, Italy

F. Romanato, A. Drigo, and A. Carnera

Dipartimento di Fisica dell'Università, INFN, via Marzolo 8, 35131 Padova, Italy

C. Brizard, J. R. Regnard, and J. L. Allain

Commissariat à l'Energie Atomique, Département de Recherche Fondamentale sur la Matière Condensée, SP2M/PI-17, rue des Martyrs, 38054 Grenoble Cedex, France

(Received 10 January 1995)

The diffusivity of antimony into silicon and its dependence on the Fermi-level position and on the structure of lattice defects has been investigated by high-dose ion implantation (2 and 5×10^{16} atoms Sb cm^{-2}). The donor concentration has been strongly increased by a subsequent pulsed laser annealing treatment. For comparison, laser annealing of samples coimplanted with the same doses of both Sb and B has been performed in order to obtain a strong electrical compensation. The heat treatment for diffusion experiments of both Sb- and Sb+B-implanted wafers have been performed at a rather low temperature (600°C for 1 h). Contrary to the prediction of the extrapolated Fair's equation, a significant shift in the dopant concentration profiles, as well as the formation of Sb precipitates, Sb-vacancy, and/or Sb-B pairing have been observed. To explain this diffusivity, a diffusion coefficient D_{Sb} , independent of the dopant concentration and seven orders of magnitude higher than that previously determined by Fair, must be assumed. This means that the increased Sb diffusivity is not related primarily to the Fermi-level position. The huge increase in D_{Sb} is related to defects (e.g., twins, dislocations, rodlike defects, precipitates, and dopant complexes) which have been characterized by extended x-ray-absorption fine-structure, Rutherford backscattering spectrometry and channeling, and TEM techniques analyses. Moreover, an anomalous high tensile strain of the samples indicates a large incorporation of vacancies. These defects are also responsible for the dopant backwards diffusion and outdiffusion, which is another surprising phenomenon which occurred during thermal annealing of most of the samples.

I. INTRODUCTION

In silicon integrated circuit technology, regions heavily doped with both donor and acceptor atoms are frequently encountered. In addition to the expected electrical compensation, a structural compensation has been also reported for III-V mixed doped silicon, which is due to the formation of dopant complexes and pairs.¹⁻⁵ An additional phenomenon, which takes place during high-temperature annealing of antimony-boron coimplanted silicon samples, is retarded Sb diffusion in the p^+ doped region with a near-uniform profile.³

In one of our recent works⁵ on codiffusion in silicon at 900 and 1000°C of B and Sb, both implanted at high dose (2×10^{16} cm^{-2}), secondary-ion-mass spectrometry (SIMS) concentration profile measurements and transmission electron microscopy (TEM) observations supported the hypothesis of mobile donor-acceptor pairs and the increase of antimony solubility through a reduction in the precipitated Sb fraction. Moreover, the diffusivity of

both dopants in codiffused samples was lower than that of the individual dopants, the Sb^+B^- pairs being mobile, though with a low diffusivity.

The purpose of this work is to investigate how Sb diffusivity is affected by a strong variation of the Fermi-level position during diffusion. Andersen *et al.*⁶ found extremely large diffusion coefficients of Sb during high-temperature rapid thermal annealings in Si wafers containing high concentrations of P donors. To achieve this situation, in our experiments a pulsed laser annealing treatment has been performed in samples heavily implanted with Sb only, and in samples coimplanted with Sb and B. In the first case, this leads to an electrically active concentration of 2×10^{21} cm^{-3} , with the Fermi level close to the conduction band, whereas in the latter samples the strong electrical compensation brings the Fermi level closer to the band-gap center. Moreover, heat treatments for diffusion experiments of both Sb- and Sb+B-implanted samples are performed at 600°C , a temperature markedly lower than the ones used by Margesin *et al.*,⁵ which should induce no shift in the correspond-

ing concentration profiles. A preliminary extended x-ray-absorption fine-structure (EXAFS) analysis of these specimens⁷ showed, rather surprisingly, that both precipitation and pair formation take place, thus indicating that the diffusivity at 600 °C should be larger than expected.³ In order to discriminate between effects induced by the carrier concentration^{3,5} and those induced by the structure of the samples, an extensive structural characterization has been performed. The use of SIMS, TEM, EXAFS, Rutherford backscattering spectrometry (RBS), nuclear reaction analysis (NRA), and ion-channeling techniques allowed us to characterize dopant concentration profiles, lattice defects, precipitates, and complexes involving Sb and B as well as the dopant lattice site location and the strain of the dopant layers.

II. EXPERIMENT

A. Specimen preparation

The effect of the coimplantation of Sb+B on Sb diffusivity has been investigated in $\langle 100 \rangle$ Si monocrystalline wafers, and has been systematically compared with corresponding Sb-only implanted case. Two implantation doses have been studied: 2×10^{16} and 5×10^{16} ions cm^{-2} . In each coimplanted sample, the Sb and B doses are nominally the same in order to maximize the coimplantation effect.⁵ The Sb^+ and $^{11}\text{B}^+$ ions have been implanted at 160 and 20 keV, respectively, in order to obtain the same impurity depth range. In fact, the projected range R_p and the straggling ΔR_p are (79.5 ± 23.3) nm for Sb and (74.9 ± 28.3) nm for B. In order to obtain a nearly constant concentration profile of the dopants, and in order to recrystallize the implanted layers, laser annealing has been performed with a pulsed excimer laser (XeCl, $\lambda = 308$ nm). The pulse duration was 40-ns FWHM, and the energy density was set at 1.8 J cm^{-2} . A computer simulation of the thermal transient under the present conditions indicates that the melt thickness exceeds 300 nm. Part of the laser-annealed wafers were then furnace annealed in a nitrogen atmosphere containing 10% oxygen at a temperature of 600 °C for 1 h.

B. Ion-beam techniques

RBS, NRS, and ion-channeling experiments were performed at Laboratori Nazionali di Legnaro by using beams accelerated by a 2-MV Van der Graaff accelerator.

The nuclear reaction yield from ^{11}B atoms was obtained by using a 630-keV proton beam, allowing us to exploit the maximum of the broad resonance in the $^{11}\text{B}(p, \alpha)^8\text{Be}$ nuclear reaction cross section.⁸ At this proton energy, the reaction probability is approximately constant from the surface to the maximum depth where B is located in the samples (300–400 nm). The yield from Sb and Si atoms was obtained simultaneously by recording the backscattered protons following the technique described in Ref. 9. As both NRA and proton RBS suffer from poor depth resolution, the results of such an analysis are relative to the whole implanted and doped layer. In order to improve the depth resolution, RBS ex-

periments were also performed using a 2.0-MeV $^4\text{He}^+$ beam to obtain the yield from Sb and Si atoms. The backscattering angle was set in such a way as to allow a depth resolution between than 15 nm. The integrated beam charge was obtained by using the whole scattering chamber as a Faraday cup, and the detection solid angle was calibrated by means of standard samples whose composition is known with an accuracy better than 2% (Ref. 10) and 5% (Ref. 11) for RBS and NRA, respectively.

For the channeling experiments the samples were mounted on a three-rotation-axis goniometer¹² with two translation axes allowing us to move the beam impact point on the sample surface in order to avoid beam-induced damage effects. Channeling dips were obtained for the [001], [101], and [111] lattice directions by tilting the incident beam direction toward a carefully chosen random direction. Depth-resolved channeling dips for Sb and Si were obtained by recording the whole ^4He RBS spectra for each angular position, and afterwards the appropriate energy windows were chosen *a posteriori* either by observing the specific dechanneling features or on the basis of the TEM observations. In the case of NRA-RBS experiments (H^+ beam), besides the α particle peak from the nuclear reaction on ^{11}B atoms the Sb and Si proton RBS yields from energy windows corresponding to the maximum Sb depth were recorded as a function of the tilt angle. Channeling experiments were also used to measure the tetragonal distortion of the doped layers following the procedure described in Ref. 12.

Secondary-ion-mass spectroscopy (SIMS) ^{11}B and Sb concentration profiles in the samples were measured by means of a CAMECA IMS-4f spectrometer at the Physics Department of the Padova University. A 5.5-keV O_2^+ primary beam rastered over a $250 \times 250\text{-}\mu\text{m}^2$ area was used for sputtering, while the positive secondary ion signals were collected from the 60- μm -diameter central area. The erosion time to depth conversion was obtained by means of a Tencor Alpha-Step 200 stylus profilometer which was used to measure the height of the sputtering crater. The secondary-ion yields were converted into atomic concentrations by using the RBS and NRA Sb and B dose data. In fact, in all samples the maximum concentrations are above 1 at. %, and the conversion obtained by conventional low-dose ion-implanted calibration standards is affected by matrix effects. In order to characterize the extension and the depth shift of the concentration profiles, we conventionally assume, as a reference, the depth where the concentration drops below 10^{19} at cm^{-3} , i.e., more than two orders of magnitude below the maximum concentrations.

C. EXAFS

The EXAFS experiments were carried out at the wiggler station 9.3 of the Daresbury synchrotron. Near-grazing-incidence geometry fluorescence EXAFS was performed at the Sb *K* edge (30 491 eV). The incident angle was approximately twice the Si critical angle (70 millidegrees at this energy). Hence the x-ray penetration

depth was approximately 500 nm; that is, larger than the Sb- and B-implanted layers. Therefore, the full implanted layer was probed during these EXAFS experiments. The high x-ray energy used explains why very few similar experiments have been carried out. To our knowledge, only Van Netten, Stapel, and Niesen¹³ performed similar EXAFS experiments on a 70-ppm Sb-implanted silicon crystal.

The fluorescence detector used was a Canberra 13 Ge diode detector with an excellent signal-to-noise ratio due to its energy discrimination. As the samples are monocrystalline, this device is also useful to eliminate the Bragg peaks present in the EXAFS spectra. The signals from the different detectors were summed all together after removal of the Bragg peaks. Several scans were performed for each sample in order to obtain better statistics.

For the EXAFS analysis, the first reference sample used was a metallic Sb foil in order to obtain Sb-Sb backscattering and phase information. This reference is appropriate because at high annealing temperatures many Sb-implanted atoms are in precipitates in the metallic Sb rhombohedral structure. Each Sb atom has three first-nearest neighbors (NN's) at 2.90 Å, and three second NN's at 3.36 Å.¹⁴ The second reference used is a 2×10^{16} Sb and B at. cm⁻² sample, for which it is supposed that each Sb atom is surrounded by four Si neighbors. Indeed, after laser annealing, the Sb atoms are in substitutional sites up to a concentration of approximately 2×10^{21} atoms cm⁻³. Bechstedt and Harrison¹⁵ theoretically estimated that the Sb-Si distance in the substitution approximation is 2.52 Å.

The EXAFS spectra have been analyzed by using the spherical wave program EXCURV.¹⁶ As the Sb atom is heavy, the backscattering amplitude is still important at high-*k* values; hence the EXAFS signal has been recorded and analyzed within a 700-eV range. Conversely, the B atom is light; hence the EXAFS backscattering amplitude is weak and limited to small-*k* values. Actually, the B atom looks like a vacancy regarding the EXAFS analysis. This effect has been shown by simulating the EXAFS spectrum of a Sb atom surrounded by either three Si atoms and one B atom or three Si atoms and one vacancy by using EXCURV theoretical backscattering amplitudes and phases. No difference has been found between the two EXAFS spectra. Therefore, no direct information is obtained for the Sb-B bond. It will be shown that the influence of B can be seen through the number of Sb atoms in precipitates.

D. TEM

TEM observations were performed at Consiglio Nazionale delle Ricerche, Istituto di Chimica e Tecnologia, dei Materiali e Componenti per l'Elettronica (LAMEL), by using a CM30 TEM/STEM operating at 300 keV. Cross-sectional TEM (XTEM) was obtained by preparing the specimens according to the conventional procedures of gluing, sawing, and mechanical polishing down to 20 micrometers and ion-beam milling to perforation.¹⁷

III. RESULTS

A. As-implanted samples

RBS-channeling analysis of the low-dose Sb as-implanted sample shows that the thickness of the Si surface amorphous layer is 216 nm. This thickness rises to 235 nm after successive B implantation. For the high-dose-implanted samples, the amorphous thickness is about 250 nm for Sb- and Sb+B-implanted samples. The Sb as-implanted doses, measured by RBS, are reported in Table I, where the acronyms used for the different samples are also explained. These doses are about 11% and 7% higher than the nominal doses for low- and high-dose samples, respectively. The reduced discrepancy for high-dose samples is attributed to sputtering. On the contrary, B postimplantation appears to have a negligible sputtering effect, and the B-implanted doses, measured by NRA, turn out to be about 3% lower than the nominal doses (see Table I), i.e., in the systematic error of the measure. SIMS concentration profiles (not shown) are approximately Gaussians with peaks at a depth of (70 ± 5) nm for both ions, the maximum concentration being about 3×10^{21} and 7.5×10^{21} at. cm⁻³ for low- and high-dose samples, respectively, and for both ions.

The EXAFS Fourier transforms (FT's) of the implanted specimens have only one peak corresponding to the first NN's [Fig. 1(a)], confirming the amorphous structure of the implanted layers. The first-NN results for the amorphous samples are reported in Table II. Whatever the implantation dose and B coimplantation or not, the Sb local environment is 3.2 Si atoms at approximately 2.60 Å. This Sb-Si distance is larger than the one corre-

TABLE I. Summary of the investigated samples and of the annealing treatments. The samples have been named according to the following scheme: the first number identifies the nominal implantation dose ($\times 10^{16}$ at cm⁻²) of the elements specified by the subsequent chemical symbols; the last letter identifies the treatment, *A*, as-implanted; *L*, laser annealed; *T*, laser + 600°C 1-h annealed. In the case of coimplantation of the elements the nominal dose is the same. The last columns report the dopant content measured by RBS (Sb) and NRA (B).

Name	Annealing process	Sb dose	B dose
2Sb <i>A</i>	as-implanted	2.20±0.03	
2B <i>A</i>	as-implanted		2.07±0.1
2SbB <i>A</i>	as-implanted	2.24±0.03	1.92±0.06
2Sb <i>L</i>	laser	2.22±0.03	
2Sb <i>T</i>	laser + therm	2.09±0.03	
2SbB <i>L</i>	laser	2.26±0.03	1.99±0.04
2SbB <i>T</i>	laser + therm	2.30±0.03	1.94±0.04
5Sb <i>A</i>	as-implanted	5.40±0.05	
5SbB <i>A</i>	as-implanted	5.37±0.05	4.86±0.06
5Sb <i>L</i>	laser	5.36±0.05	
5Sb <i>T</i>	laser + therm	4.95±0.05	
5SbB <i>L</i>	laser	5.34±0.05	4.83±0.06
5SbB <i>T</i>	laser + therm	4.93±0.05	3.91±0.06

TABLE II. Results of the EXAFS analysis. N , R , and $2\sigma^2$, respectively, are the number, the distance, and the Debye-Waller factor of the first NN's around Sb.

Sample name	N		$2\sigma^2$ (\AA^2)	R (\AA)	
	Si	Si		Sb	Sb
2SbA	3.3	2.61	0.014		
2SbBA	3.2	2.58	0.006		
2SbL	4.4	2.54	0.008		
2SbT	3.9	2.55		0.4	2.82
2SbBL	4	2.54	0.006		
2SbBT	3.8	2.54			
5SbA	3.2	2.59	0.014		
5SbBA	3.1	2.59	0.011		
5SbL	3	2.56	0.007		
5SbT	1.1	2.59		1.4	2.87
5SbBL	3.1	2.54	0.007		
5SbBT	2.2	2.55		0.2	2.85

sponding to substitutional Sb surrounded by four Si neighbors.¹⁵

B. Low-dose samples

The SIMS concentration profiles of the dopants in the annealed low-dose samples are reported in Figs. 2(a) and 2(b) for the Sb- and Sb+B-implanted samples, respectively.

As a consequence of the laser annealing process, the Sb and B concentration profiles exhibit the expected features. In fact, as-implanted profiles have been redistributed nearly uniformly in a surface layer where the con-

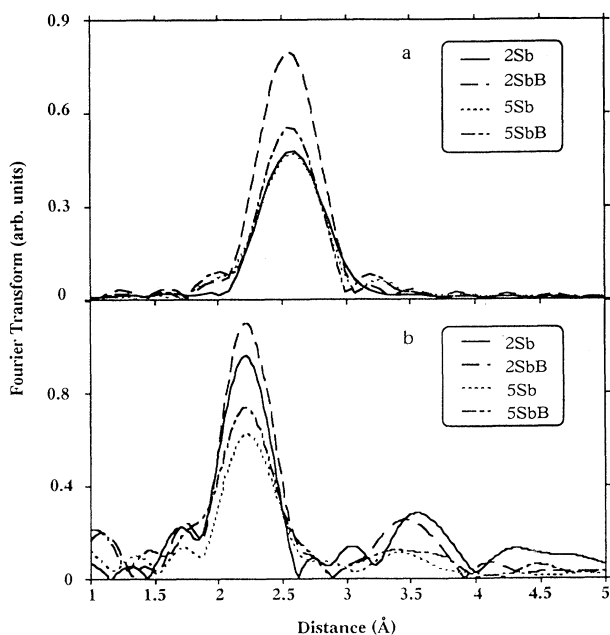


FIG. 1. Fourier transform of the EXAFS spectra of (a) the as-implanted and (b) the laser-annealed samples.

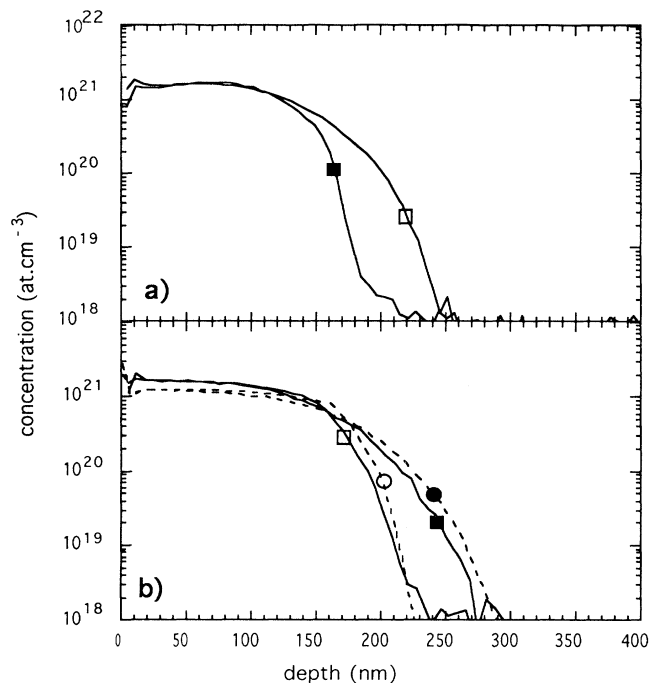


FIG. 2. SIMS concentration profiles of the low-dose samples: (a) samples 2SbL and 2SbT; (b) samples 2SbBL and 2SbBT. Solid lines and squares refer to Sb concentration profile, while the hatched line and circle to B; open and full symbols refer to samples before and after thermal annealing, respectively.

centration varies from 1 to 2×10^{21} at cm^{-3} . Moreover, this uniform composition layer is followed by a tail extending to depths equal to or larger than those of the as-implanted amorphous layer, confirming that the laser annealing process leads to the melting of at least all the amorphous layer, allowing subsequent epitaxial regrowth from the crystalline substrate. The Sb and B profiles in the coimplanted sample are nearly the same as expected for a diffusion in the liquid phase.

As a consequence of our low temperature thermal annealing process (600 °C), no appreciable Sb diffusion is expected. Conversely, both Sb-implanted and coimplanted samples show large modifications in the concentration profiles. The most striking feature is exhibited by the Sb-implanted sample, where the diffusion proceeds outwards, i.e., against the concentration gradient, and is accompanied by a significant (7%) Sb loss (see Table I). In the case of the coimplanted sample, the diffusion proceeds inwards and nearly to the same extent for Sb and B. In this case no dopant loss is observed. The percentage of dopant loss and the concentration profile shift (difference in 10^{19} at. cm^{-3}) are reported in Table III, where the most important structural features of all the investigated samples are summarized as well.

The weak beam dark-field (WBDF) XTEM micrograph of sample 2SbL is reported in Fig. 3(a). It shows a highly defective region which extends from the surface down to a depth of 80 nm and consists of vertical dislocations and

TABLE III. Summary of the main results of the different techniques. The SIMS columns show, for every thermal annealed sample, the dopant fraction outdiffused and the profile tail displacements (at 10^{19} at cm^{-3}) taking as the reference (ref.) the corresponding laser annealed sample. The negative sign indicates a displacement towards the surface. The EXAFS columns report the fraction of Sb atoms that have different first-NN configurations: (*T*) tetrahedral Si first NN's, (*C*) complexes two Si first NN's, (*P*) Sb precipitates 3 Sb NN's. The Channeling columns report the experimental and computed values of the parallel strain, ϵ_{\parallel} , the substitutional fraction of the dopants, *S*, and the relative average static displacements, $\Delta r/\rho$, of the Si matrix and of the dopants. In the case of depth-resolved analysis, each row corresponds to a given layer whose depth range and content (dopant fraction) are reported in the respective columns. The presence of precipitates detected by channeling is indicated by *P*. The TEM column reports the main morphological features of each layer. The asterisks refer to measurements impaired by a large dechanneling given by the upper layers, thus resulting in not fully reliable data.

Sample	Sb		Sb		Sb		Sb		Channeling		Depth range (nm)	Dopant fraction	TEM
	Surface outdiffusion [%]	Shift tail [nm]	Surface outdiffusion [%]	Shift tail [nm]	EXAFS T	EXAFS C	EXAFS P	ϵ_{\parallel} expt. (10^{-3})	ϵ_{\parallel} calc.	S_{Sb}			
2SbL	ref.	ref.	1.0	0.0	0.0	+1.0	-5.0	0.94	*	*	0-230	1.00	threading disl. + point defect cluster
							0.92*		*	*	0-80	0.57	no extended defects
							0.94		0.6	1.2	80-160	0.39	rod-like defects
2SbT	7	-50	0.9	0.0	0.1	+0.1	-5.0	0.67*	*	*	160-200	0.04	thread. disl.
							0.70*		*	*	0-200	1.00	point defect cluster, Sb precipitates
							0.61		0.5	1.6	45-130	0.66	point defect cluster, disl. loops
2SbBL	ref.	ref.	1.0	0.0	0.0	+4.0	+1.0	0.98	1.0	≤ 1.0	130-170	1.00	no extended defects
2SbBT	0	+50	0	0.9	0.1	+4.3	+1.0	0.96	0.7	1.2	0-260	1.00	no extended defects
5SbL	ref.	ref.	0.5	0.5	0.0	*	*	0.64*	*	*	0-230	1.00	twins + point defects cluster
							0.62*		*	*	0-120	0.90	no extended defects + point defects cluster
							0.66*		*	*	120-230	0.10	twins + Sb precipitates
5SbT	9	-40	0.0	0.5	0.5	*	*	*	*	*	0-100	0.79	no extended defects + point defects cluster
							0.20*		*	*	100-220	0.21	twins + threading disl.
5SbL	ref.	ref.	0.5	0.5	0.0			0.89	0.9	1.2	0-340	1.00	no extended defects
							0.8*		*	*	0-90	0.51	no extended defects
							+6.3*	+3.0*	0.6	1.1	90-340	0.49	twins + precipitates
5SbT	9	-30	19	-45	0.2	0.7	0.1	0.82	0.9	1.6	0-300	1.00	no extended defects
							0.77*		*	*	0-90	0.67	twins + precipitates
							+3.7*	0.0*	0.6	1.3	90-300	0.33	no extended defects

small dots. The dislocations are probably related to a columnar regrowth of the implanted layer, due to instabilities in the solid-liquid interface,¹⁸ the column boundaries being decorated with Sb. The small dots are probably clusters of point defects. The existence of this defective region indicates that, even for the lower Sb dose, the laser treatment is unable to fully recover the crystal structure of silicon up to the surface of the wafer. It is also possible to see, in Fig. 3(a), a band of small defects,

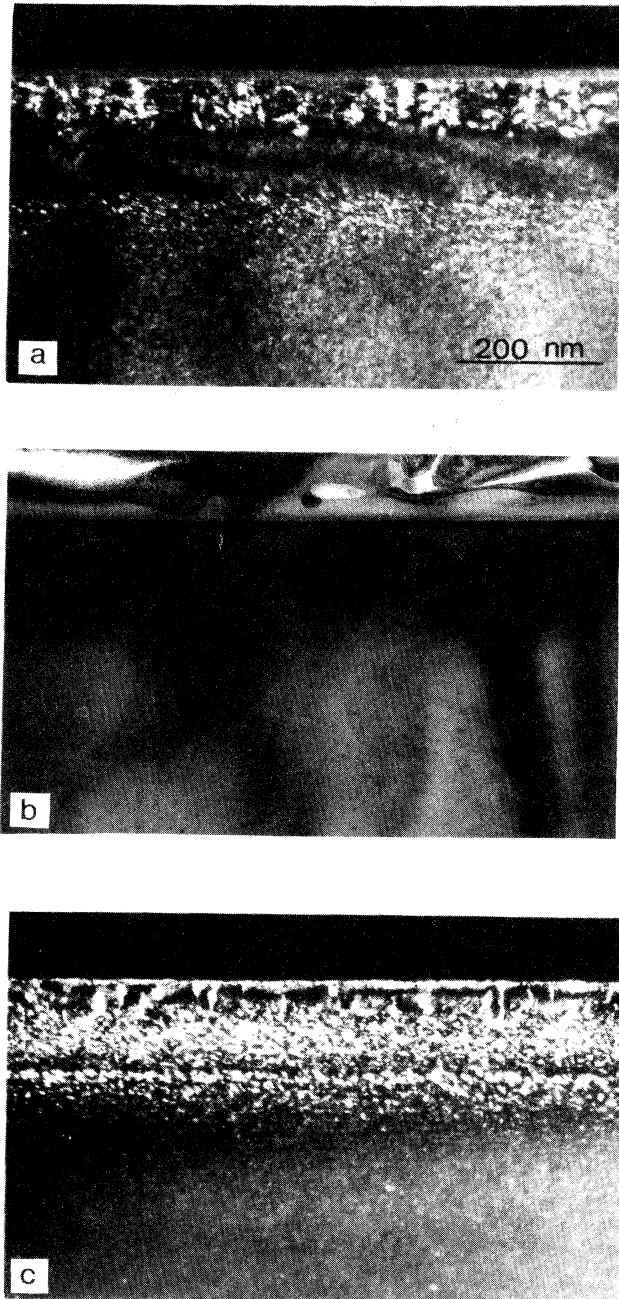


FIG. 3. TEM micrographs taken in the lower-dose samples (a) 2SbL, WBDF; (b) 2SbBL, BF, (c) 2SbT, WBDF.

located at a depth of 180 nm. A closer inspection by high-resolution transmission electron microscopy (HRTEM) reveals that they are rodlike defects (RLD), i.e., (113)-oriented Si platelets.¹⁹

In order to compare the effect of the coimplantation, in Fig. 3(b) the bright-field XTEM image of sample 2SbBL is reported. No extended defects are observed, indicating that the simultaneous presence of B strongly favors the crystal regrowth. The subsequent thermal annealing of this sample does not induce any observable TEM change in the structure.

The effect of the thermal annealing on the Sb-implanted and laser-annealed sample is shown by the WBDF XTEM image of sample 2SbT reported in Fig. 3(c). The depth of the surface layer containing threading dislocations is reduced to 45 nm, and the dislocation density is reduced with respect to the laser-annealed sample [compare Fig. 3(a)]. At a larger depth, there is a band, 85 nm wide, consisting of a large population of small defects, which in part includes small Sb precipitates, as found by channeling experiments in the corresponding depth region and also by EXAFS (see below). Evidence of these precipitates is given by a weak polycrystalline ring in the diffraction patterns (not reported here) taken in that region, whose interplanar spacing corresponds to that of (102) planes of hexagonal antimony. Deeper in the crystal, there is a high concentration of similar small defects, peaked around 145 nm. This depth corresponds to the position of the Si defects observed by channeling (see Fig. 6), thus indicating that they probably consist of small dislocation loops.

Let us start the description of the channeling analysis with the best regrown samples, i.e., the coimplanted samples. After laser annealing the depth-resolved channeling analysis performed by employing a 2.0-MeV He⁺ beam does not show any significant depth feature, and the results are in perfect agreement with those obtained by using a 0.63-MeV H⁺ beam, including the expected beam energy scaling for the critical angle. The aligned spectra closely resemble those of a perfect crystal. The channeling analysis has been repeated for the three principal lattice directions, i.e., [001], [101], and [111] axes. The Sb, B, and Si dips for the [101] axis of sample 2SbBL are shown in Fig. 4, and compared to that obtained for virgin Si. The channeling dips for Sb and B are identical, and they differ from the dip relative to the Si matrix only for a slightly higher minimum yield. The same result has been obtained for all the investigated directions.

The substitutional lattice location of an impurity leads to channeling dips with the same width for the host matrix and the impurity as in the present case. The shadowed fraction of the impurity atoms is then easily extracted by comparing the minimum yield χ of the two signals:²⁰

$$S = \frac{1 - \chi_I}{1 - \chi_M}, \quad (1)$$

where χ_I and χ_M are the normalized minimum yield of the impurity and of the host matrix, respectively. For a substitutional location the shadowed fraction is indepen-

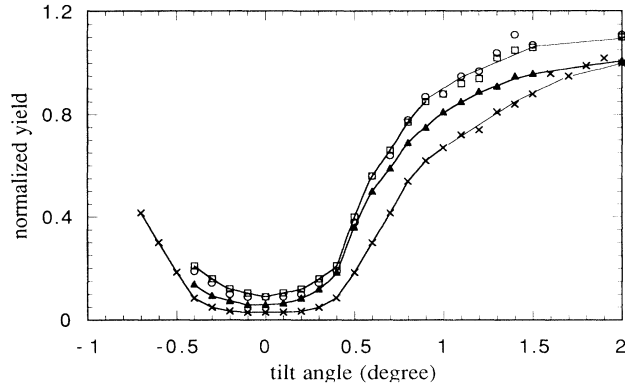


FIG. 4. 0.63-MeV H^+ beam [101] angular scan of sample 2SbBL. \times , RBS on a virgin Si crystal; \blacktriangle , RBS on the Si matrix of the sample; \square , RBS on Sb; \circ , NRA on B. The lines are only drawn to guide the eye.

dent of the channeling direction and equal to the substitutional fraction. From our data it appears that both Sb and B atoms are 98% substitutional in the Si lattice.

However, we must notice that the dip of the matrix shows a smaller (about 10%) critical angle and a higher minimum yield than the dip of virgin Si. This fact can be interpreted by a *distortion* of the Si lattice caused by the high concentration of dopants with different bond length with respect to Si. The actual Si displacements could be investigated by using extensive Monte Carlo simulations which are out of the scope of this work. However, a semi-quantitative estimate of the displacements can be made in the framework of the Lindhard continuum potential model.²¹ Let us consider the atomic distribution around the lattice string in the transverse plane. In a perfect crystal, the position of each atom has a Gaussian distribution, centered on the lattice site, with a standard deviation equal to the rms transverse thermal vibration amplitude, ρ . Random static displacements in the atomic equilibrium positions lead to a further broadening of the transverse distribution of the atom rows and to a corresponding narrowing of the channeling dip as if the thermal vibration amplitude was increased. By comparing the experimental critical angles of the Si matrix and of a virgin Si crystal, the static broadening Δr_M of the Si atoms can be derived.²⁰ A dopant dip narrower than that of the Si matrix indicates that the dopant transverse distribution is broader than that of the matrix atoms. In this case the distribution width Δr_{dop} can be obtained by the same procedure as above. The results of this procedure are reported in Table III for the [001] case, even though limited to the crystal regions where extended defects are not revealed by TEM.

It is worth noting that the static displacement values are well above the error bar and of the order of ρ , i.e., about 0.1 Å, perpendicular to the [001] direction. If the actual atomic displacements are assumed to be in the $\langle 111 \rangle$ directions, along which the covalent bond is directed, a displacement of the order of 0.2 Å is obtained. This value agrees very well with the difference in bond

length between Si—Si (2.35 Å) and Si—Sb (2.54 Å) or Si—B (2.06 Å) thus giving meaning to the above analysis.

By looking at the Δr values in Table III it appears that nowhere but in sample 2SbBL can lattice sites occupied by Sb and B be considered perfectly substitutional. Moreover, the Si matrix is always distorted so that the concept itself of *perfectly substitutional* becomes somewhat ambiguous. Nevertheless, in most cases the displacements are small so that, for simplicity, we shall refer to these dopant off-center site locations as substitutional sites (in the distorted matrix). As the effect of the off-center site occupation is not only to narrow the dip but also to increase the minimum yield, it follows that the substitutional fraction calculated through Eq. (1) must be considered as a lower estimate of the actual value. The substitutional fractions calculated by using Eq. (1) are reported in Table III.

By comparing the SIMS concentration profiles and the results of the substitutional fraction, it appears that both dopants are in substitutional position up to a concentration of nearly $2 \times 10^{21} \text{ cm}^{-3}$. This huge amount of substitutional dopants can be obtained by the nonequilibrium process of the liquid-phase epitaxy by laser annealing treatment.

As a consequence of the thermal annealing on the coimplanted sample (2SbBT), the substitutional fraction of both B and Sb does not change. However, a certain reordering of the Si matrix accompanied by a significant displacement of the dopants is observed (see Δr data in Table III). It must be noted that dopant precipitation does not occur despite the very large supersaturation of both dopants; in fact, the solid solubility at 600°C is less than $1 \times 10^{19} \text{ cm}^{-3}$ for both Sb (Ref. 22) and B (Ref. 23).

The TEM investigation of the Sb-implanted samples showed the presence of three layers with different defects. As a consequence, the channeling analysis has been correspondingly depth resolved and the results are reported in Table III. As far as the substitutional fraction is concerned, the integral analysis of the whole implanted layer is also reported for the sake of comparison with the EXAFS data.

In Fig. 5(a) we report the [001] channeling dips of sample 2SbL recorded in the intermediate layer (80–160 nm), where TEM does not reveal any defect. The Sb and matrix minimum yields are much higher than that of the reference virgin Si because of the dechanneling in the surface layer where a high density of extended defects is present. Nevertheless, the result for the Sb substitutional fraction is very close to that of the corresponding coimplanted sample, indicating that a Sb concentration of $2 \times 10^{21} \text{ cm}^{-3}$ in substitutional sites is achieved after laser annealing even without coimplantation.

A different behavior is shown in the region where TEM suggests the presence of rodlike defects. The channeling dip for the layer between 160 and 200 nm, shown in Fig. 5(b), indicates that the Sb critical angle is only 60% of that of the matrix. Nevertheless, the minimum yield is the same as the one of the matrix. These facts lead to the conclusion that Sb precipitation, partially coherent with the Si matrix, occurs in this layer. This fact could be connected to the RLD decoration, but the present mea-

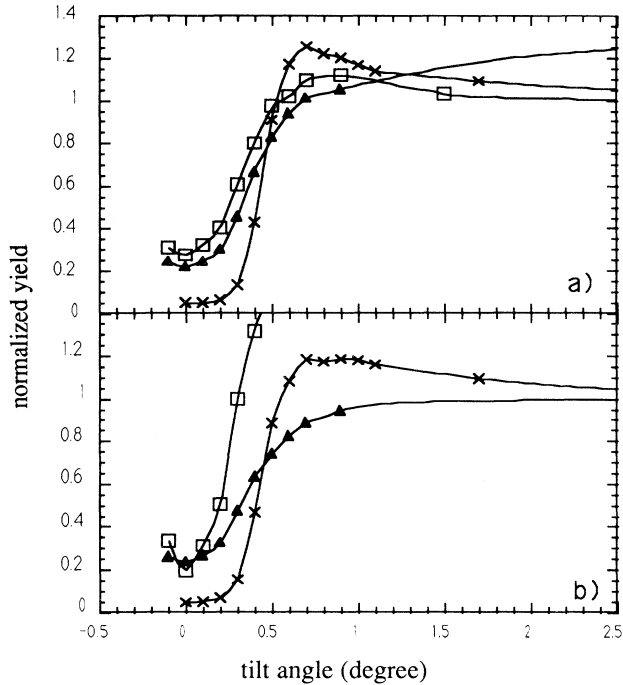


FIG. 5. 2.0-MeV He^+ beam RBS depth-resolved [001] channeling dips of sample 2SbL and of a virgin silicon crystal; (a) 80–160-nm depth range; (b) 160–200-nm depth range. The meaning of the symbols is the same as in Fig. 4.

measurements cannot exclude Sb precipitation in the crystalline regions between RLD's.

The Δr_{Sb} value in this layer is very high, and probably the corresponding analysis becomes too approximate. The values are reported in Table III as a marker of the precipitate presence.

After the thermal annealing (sample 2SbT) the situation is markedly different. The 2.0-MeV He^+ random and [001] channeling spectra of this sample are shown in Fig. 6. The main feature in the aligned spectrum is the Si

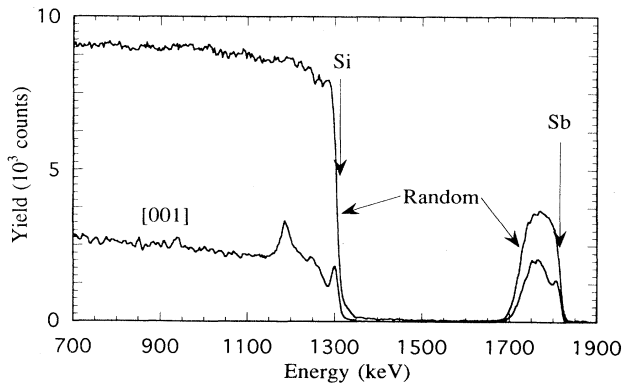


FIG. 6. 2.0-MeV He^+ RBS spectra of sample 2SbT collected in the random direction and in the [001] channeling condition. The vertical arrows show the surface backscattering energy from Si and Sb atoms.

damage peak at about 1180 keV, corresponding to a depth of 160 nm, i.e., in the region where TEM suggests the presence of small dislocation loops. Channeling angular yield analysis shows that at any depth the Sb dip is narrower than that of the matrix, while the Sb minimum yields are higher. These facts indicate that the effect of the thermal annealing has been to displace most of the Sb atoms from regular lattice sites. In fact, the Δr_{Sb} values suggest the presence of precipitation even in the layer where no extended defects are present. A clear indication of Sb precipitates partially coherent with the Si matrix is found again in the tail region of the concentration profile (130–180 nm).

Finally the measured channeling values of the parallel strain are also reported in Table III. Surprisingly, it appears always to be positive (tensile) even when only Sb is implanted and a compressive stress is expected. The expected surface strain values can be computed in the assumption that extended defects causing plastic relaxation are absent in the epitaxially regrown layer, and by considering the lattice expansion (contraction) caused by the inclusion in substitutional sites of atoms with larger (smaller) covalent radius than the matrix atoms. It turns out that

$$\epsilon_{\parallel} = c_{\text{dop}} \frac{r_{\text{Si}} - r_{\text{dop}}}{r_{\text{Si}}}, \quad (2)$$

where c_{dop} is the dopant relative concentration obtained from the SIMS dopant profiles, and r_{dop} and r_{Si} are the covalent radii of the dopant atom and of Si, respectively. The covalent radius of Si is deduced by the lattice parameter of pure Si. For the covalent radius of B the empirical value given by Pauling²⁴ (0.88 Å) has been used, while for Sb the present EXAFS value (1.364 Å) has been adopted. It must be noted that this value is in good agreement with that deduced from the linear expansion coefficient measured in Ref. 25. The expected strain values are reported in Table III for comparison with the experimental values as well.

The EXAFS FT's of the laser-annealed samples are shown in Fig. 1(b). The recrystallization of the implanted layer is evident: a clear second-NN peak exists at 3.84 Å. This distance is characteristic of the second NN in monocrystalline Si. No Sb-Sb first-NN contribution has been found. The EXAFS results are reported in Table II. Whatever the sample, the Sb-Si distance is approximately 2.54 Å. This value is consistent with the theoretical one calculated by Bechstedt and Harrison¹⁵ (2.52 Å) and the one measured by EXAFS by Van Netten, Stapel, and Niesen¹³ in a 70-ppm Sb-doped Si crystal (2.53 Å).

For the low-dose samples the first-NN number is approximately 4 and, only in the case of sample 2SbT, a peak corresponding to Sb-Sb couples, with a very low coordination number (0.4), was found. These features, together with the information obtained by TEM and channeling, on one hand justify the choice of sample 2SbBL as the EXAFS reference sample for substitutional Sb; on the other hand they show that, for the low-dose Sb-implanted samples, the Sb lattice location is mainly substitutional in the Si lattice, with some Sb precipitation in the case of the thermal-annealed sample (2SbT). A more detailed

analysis will be presented below analyzing the high-dose-implanted samples.

C. High-dose-implanted samples

The SIMS concentration profiles of the dopants in the laser-annealed high-dose samples are reported in Figs. 7(a) and 7(b) for Sb- and the Sb+B-implanted samples, respectively. While in the case of Sb implantation (sample 5SbL) the concentration profile extends to nearly the same depth as in the case of the low-dose-implanted samples, the effect of the coimplantation (sample 5SbBL) is now to enhance the diffusion of both dopants greatly. To our knowledge this effect has been never observed before, and could be due to a lower melting temperature, to a smaller surface reflectivity, and/or to variations in the thermal conductivity induced by the high-B concentration. As a matter of fact, reflectivity measurements in the as-implanted specimens have shown that it decreases from 55% for the Sb-implanted sample (5SbA) to 37% for the coimplanted sample (5SbBA). This fact implies that a deeper melted front is achieved in the 5SbBA sample, and that the surface remains molten for a longer

time, allowing a deeper diffusion of the dopants in the liquid phase.

In these laser-annealed samples, the maximum concentration of the dopants is reached at a surface layer of 100 nm. The Sb concentration is roughly 4 and 3.5×10^{21} at. cm⁻³ for samples 5SbL and 5SbBL, respectively, i.e., nearly twice the concentration in the low-dose samples, while the B concentration is about 2.5×10^{21} at. cm⁻³, owing to the lower implantation dose (Table I) and to the deeper diffusion.

The thermal annealing for both types of samples leads to an outward diffusion accompanied by a significant dopant loss. In the case of the Sb-implanted sample (5SbT) the concentration tail shift is of about 35–40 nm and the Sb loss is 9%. In the inset of Fig. 7(a) the concentration profile is reported on a linear scale, allowing us to show an anomalous peak occurring around 110 nm, which is related to some kind of Sb segregation (see the TEM analysis below), and a near-surface concentration peak which is a marker of the outdiffusion process.

In the case of the coimplanted sample the concentration tail shift is of 30 and 45 nm for Sb and B, respectively. The higher-B diffusivity is also consistent with the

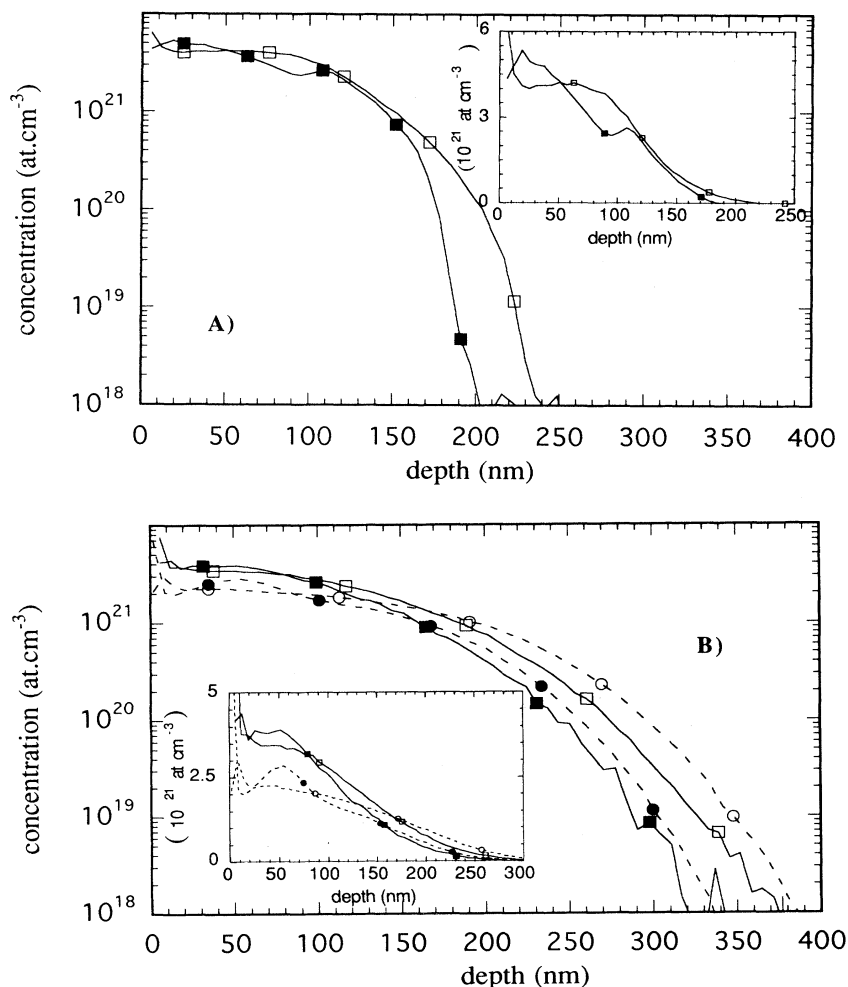


FIG. 7. SIMS dopant concentration profile of the high-dose samples: (a) samples 5SbL and 5SbT, (b) samples 5SbBL and 5SbBT. The meaning of the lines and symbols is the same as in Fig. 2.

higher dopant outdiffusion, which is 19% for B and 8% for Sb (see Table I). In the inset of Fig. 7(b) the concentration profiles are reported on a linear scale in order to better show the B near-surface (55 nm) peak, which is again an important marker of the backward diffusion and of the outdiffusion processes.

As already seen in the low-dose Sb-implanted sample, laser annealing is unable to recover perfectly the lattice

structure owing to the high-Sb concentration. Even more, TEM analysis confirms that this happens in the high-dose Sb-implanted sample 5SbL, where the Sb concentration is nearly three times greater. In fact, in this sample extended defects are present, as shown in the micrographs of Figs. 8(a) and 8(b). They consist mainly of twins up to a depth of 100 nm [Fig. 8(a)]. A high density of clusters of point defects is also present, extending from

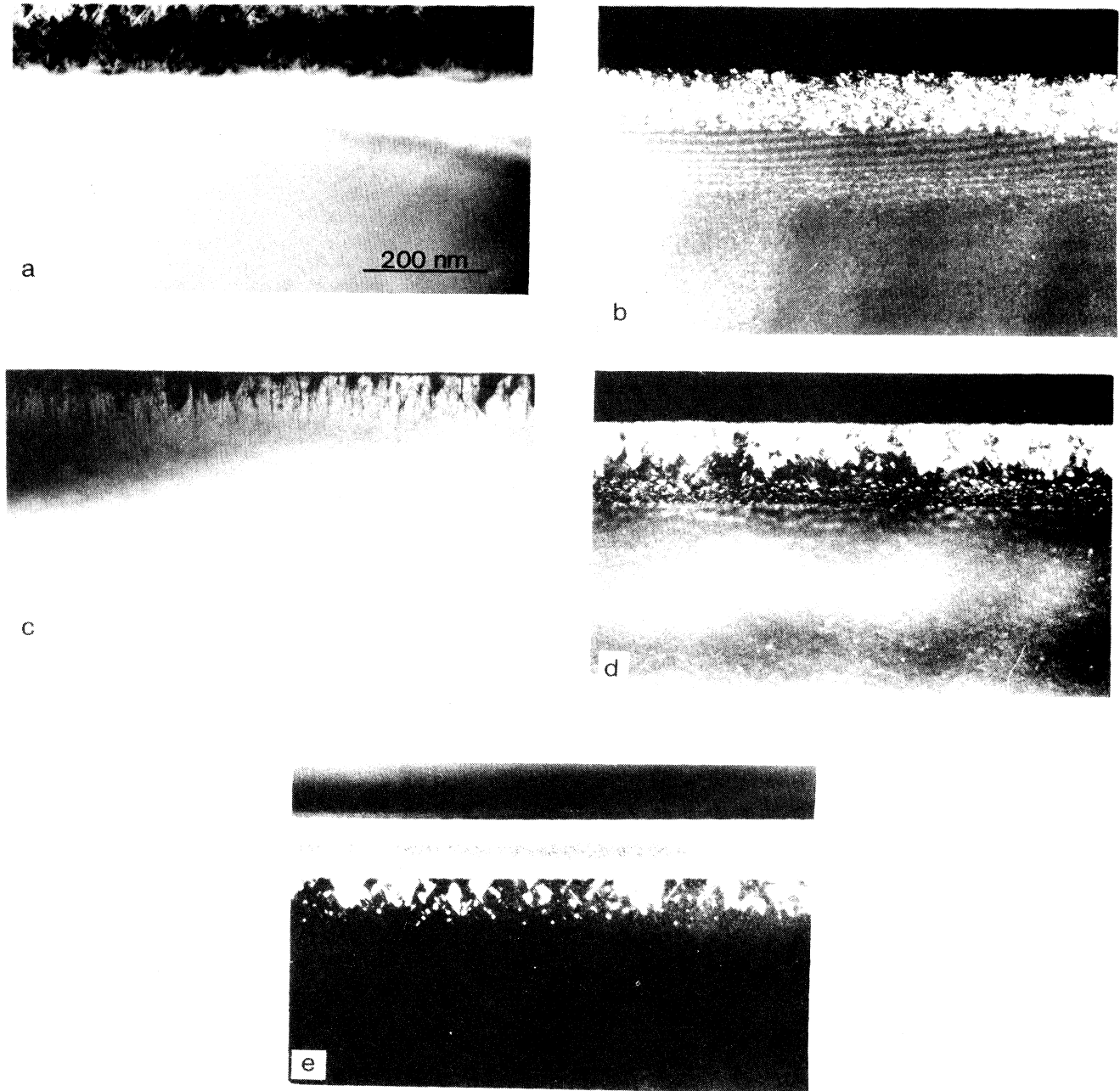


FIG. 8. TEM images taken on the higher-dose samples. (a) 5SbL, BF; (b) 5SbL, WBDF; (c) 5SbBL, BF; (d) 5SbT, DF; and (e) 5SbBT, DF. The last two micrographs have been obtained by including spots from the twins and the Sb precipitates in the objective aperture.

the surface to 120 nm, as shown by the WBDF micrograph in Fig. 8(b). Moreover, deeper in the sample, there is a band (from 210 to 230 nm) of small defects quite similar to the RDL observed in the sample 2SbL [Fig. 3(a)].

When boron is coimplanted (sample 5SbBL), the surface band of defects evolves as shown in Fig. 8(c). It spans over a range of about 90 nm and consists of threading dislocations and twins. The twin density is markedly lower than the one observed in the case of Sb-only implantation [see Fig. 8(a)], and shallower (maximum depth of about 60 nm). This is once again due to the stress compensation induced by the boron coimplantation. Moreover, as in the low-dose case, the deep defects observed in the 5SbL sample have disappeared.

When the high-dose samples are thermally annealed, TEM reveals that the twins, which were formed during the laser annealing, are still present, though, in the case of the 5SbT sample, for a reduced depth extension [100 nm instead of 120 nm; see Fig. 8(d)]. For the coimplanted sample, the main effect has been to annihilate the threading dislocations [Fig. 8(e)]. In addition, Sb precipitation occurs in both samples, due to the high supersaturation [Figs. 8(d) and 8(e)]. This feature is evident in the dark-field TEM micrograph in Figs. 8(d) and 8(e), taken with an objective aperture, including spots from both the twins and the hexagonal Sb precipitates. The density of precipitates is somewhat lower in sample 5SbBT than in sample 5SbT, in agreement with the EXAFS results (see below). Moreover, in sample 5SbT their extension is deeper, reaching 150 nm.

The location of the defects in the thermal-annealed sample is consistent with the results of SIMS experiments [see Fig. 7(a)]: the main peak in the profile corresponds to the twin-rich region. Moreover, in sample 5SbT the small peak at 110 nm indicates a local enhancement of the Sb concentration, due to the observed precipitates. Finally a WBDF image (not reported here) taken in sample 5SbT reveals the presence of a 20-nm-wide band of small defects, occurring beyond a depth of 220 nm, and having a size a bit larger than the ones observed before the thermal treatment [Figs. 8(a) and 8(b)]. These are clearly Si defects, as the dopant profile stops at 200 nm.

As far as the channeling analysis of the high-dose Sb-implanted samples is concerned, the high density of defects in the surface region makes it difficult, and in some cases meaningless. In Fig. 9 the random and [001]-aligned RBS spectra for sample 5SbL are reported. It appears that nearly no channeling occurs in the surface region because of the high dechanneling rate caused by twins. Moreover, it also affects the minimum yield deeper in the crystal. This is the reason why the substitutional fractions of sample 5SbL, reported in Table III, are greatly underestimated, and why they must be considered qualitative ones.

The situation becomes even worse after the thermal annealing (sample 5SbT) because of Sb precipitation. As a matter of fact, channeling occurs in a region where only 20% of the dopant is present and with a very low substitutional fraction. Nevertheless, by comparing the Sb substitutional fractions of the two samples beyond the sur-

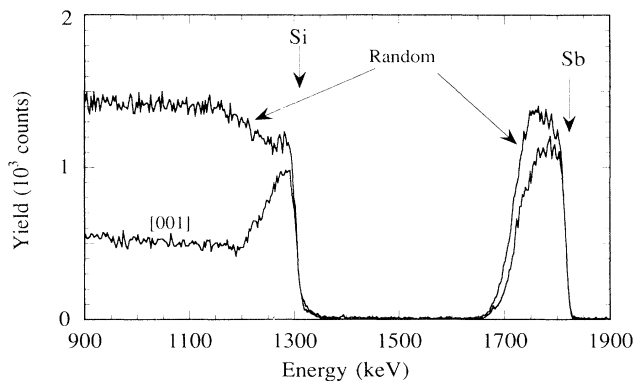


FIG. 9. Random and [001]-aligned RBS spectra of sample 5SbL.

face layer, a clear indication of Sb precipitation is obtained.

In the case of coimplanted samples the crystalline quality is much better, allowing a meaningful channeling analysis. First of all, the depth-resolved analysis for Sb shows that the substitutional fraction in the defected surface region is lower than the integral value, while in the layer below the surface defects it is comparable to that of the corresponding low-dose samples, in agreement with the fact that the Sb concentration has fallen below $2 \times 10^{21} \text{ cm}^{-3}$, i.e., the concentration in the low-dose samples. Moreover, the H^+ analysis over the whole doped layer indicates the same substitutional fractions for Sb and B as in the low-dose samples, suggesting that the B behavior is the same as that for Sb. The thermal annealing appears to cause a nearly 10% precipitation of both dopants in the region where extended defects are present. The B precipitation is further supported by the Δr_B value, which is equal to that of Δr_{Sb} and higher than the value before annealing.

The high values of the Sb and B substitutional fractions in the high-dose sample require some comments. In fact, electrical measurement of carrier concentration profiles of the 2SbL and 5SbL samples (unfortunately, donor-acceptor compensation in the coimplanted samples prevents meaningful electrical analysis), previously performed,⁷ shows that the maximum concentration of electrically active Sb is about $2 \times 10^{21} \text{ cm}^{-3}$ in both samples. In the case of sample 5SbL, it is lower than that deduced from the channeling substitutional fractions and from the SIMS dopant concentration. This fact indicates that part of the atoms in substitutional sites are electrically inactive and that, therefore, some passivating dopant complexes were formed.

The strain measurements in these samples are relative to the region where the dopant concentration begins to fall, so that the data are only qualitative. However, they are reported because they show that experimental values are again more tensile than expected. Finally, in this case thermal annealing causes a strain reduction probably connected to the dopant precipitation.

According to the EXAFS result, in all samples the Sb-

Si NN distance is consistent with that found in the case of the low-dose samples, although the average value is 2.56 Å instead of 2.54 Å. The main difference is shown by the coordination number, which is about 3 after laser annealing and even lower after the thermal annealing. In the latter case there is also evidence of some Sb-Sb NN; see Table II.

Considering sample 5SbL, as the Sb concentration is nearly twice the maximum carrier concentration obtainable by the laser-induced liquid-phase recrystallization, it can be argued that only one-half of the Sb atoms can be tetrahedrally coordinated with Si atoms. From the EXAFS average coordination number it then follows that nearly one-half of the Sb atoms must be surrounded by two Si atoms and two vacancies. These Si_2SbV_2 complexes have already been suggested by Nylandsted-Larsen *et al.* from Mössbauer experiments.²⁶ The EXAFS results do not change in the case of the corresponding coimplanted sample. To explain the data in this case, complexes involving B (Si_2SbB_2 or SiSbBV) can also be invoked, as suggested by Culbertson and Pennycook²⁷ and Margesin *et al.*⁵

Even though in principle the EXAFS technique cannot supply information about the atomic lattice site location, by considering all possible NN configurations the Sb lattice location can be inferred. In our analysis, by considering previous results, three possible configurations are considered: (i) Sb in a substitutional site (four Si NN at 2.54 Å), (ii) Sb in a complex (two Si NN at 2.54 Å), and (iii) Sb in metallic precipitates (three Sb NN at about 2.90 Å). The respective Sb fractions are called *T* (tetrahedral), *C* (complex), and *P* (precipitate), and can be obtained by solving the following set of equations:

$$\begin{aligned} 3P &= N_{\text{Sb-Sb}} , \\ 4T + 2C &= N_{\text{Sb-Si}} , \\ T + C + P &= 1 , \end{aligned} \quad (3)$$

where the experimentally determined average coordination numbers are used. The overall error on the obtained fraction values is on the order of 0.1–0.2. The results of this analysis are reported in Table III, where they can be compared to the channeling results.

IV. DISCUSSION

Before discussing the most anomalous of our results, i.e., the large and unexpected dopant diffusivity, let us summarize the main structural properties of the samples. From the results presented it clearly appears that, under laser annealing, B coimplantation leads to a much better regrowth behavior with respect to the Sb-implanted samples. This fact, of course, is a consequence of the strain reduction induced by B. As a consequence of the regrowth from the liquid phase, a boxlike dopant profile is obtained with a nearly constant concentration in a surface layer. The dopant concentrations largely overcome the solid solubility limit at room temperature for both implanted doses. The successive low-temperature thermal annealing produces some extended defect reduc-

tions, an increase of the dopant static displacements from substitutional lattice position,⁵ and an increase of the dopant complex fraction and/or of dopant precipitation, owing to the large supersaturation.

The channeling results indicate that in the coimplanted samples the substitutional fraction and the Δr values are the same for the two dopants, indicating some dopant coupling. Moreover, in the low-dose-coimplanted samples a complete substitution is obtained after the laser annealing, and maintained after the thermal annealing, despite the large B supersaturation. This result is not surprising in view of the nonequilibrium process involved in the laser annealing, while the pairing hinders the precipitation of both Sb and B in the 2SbBT sample. In fact, after thermal annealing a perfect lattice regrowth is obtained as well (2SbBT). For the corresponding high-dose samples, where extended defects are present, some Sb and B precipitation, increasing after thermal annealing, is evident also after laser annealing. In the case of Sb implantation at low dose a good regrowth, accompanied by a high-Sb substitutional fraction, is obtained after laser annealing, the successive thermal treatment causing a large precipitation. In the case of the high-dose samples, unfortunately, the occurrence of a large density of twins makes it impossible to achieve a meaningful channeling analysis.

Strain measurements always give higher values than expected. Moreover, in the case of Sb implantation, where a compressive stress is expected, a tensile strain is found. In order to explain these results it is necessary to assume that a large number of vacancies have been incorporated into the crystal during the liquid-phase regrowth. On the other hand, in the case of samples 2SbL and 2SbT, EXAFS results indicate that no Sb-V complexes are formed. Thus it appears reasonable to assume that the vacancies are related to some Si-V complex. This hypothesis could also explain the high distortion of the Si matrix observed by channeling.

The most important EXAFS result is the clear indication of Sb complex formation, particularly evident in the high-dose samples. By comparing the EXAFS and channeling results it can be concluded that the Sb atom in a complex is in a substitutional site. In fact, the sum of the *T* and *C* EXAFS fractions fits very well the channeling substitutional fraction within the respective errors. As for the structure of the Sb complexes, it clearly appears that they are SbV_2 in samples 5SbL and 5SbT, where B is not present.

In the coimplanted samples the possible formation of SbB_2 or SbVB complexes could be inferred from the evolution of the complex fraction and from the increase of the dopant Δr values after thermal annealing. In fact by looking at the EXAFS data for the high-dose Sb-implanted samples, it appears that the effect of the thermal annealing is to cause the precipitation of the former substitutional fraction, leaving the complex fraction unaffected. Conversely, in the case of the corresponding coimplanted samples, a much lower Sb precipitation accompanied by an increase of the complex fraction is observed. However, the lack of sensitivity of the EXAFS technique in the discrimination between vacan-

cies and B atoms and the impossibility, for the channeling technique, to recognize the mutual coordination of the dopants do not allow us to reach a definite conclusion.

The most striking feature of the present experiment is undoubtedly the significant Sb diffusivity at 600 °C (Figs. 2 and 7). This is not accounted for by the extrapolation at 600 °C of the Sb diffusion coefficients reported in literature.^{3,5,28} The extent of the profile shifts and of the outdiffusion observed in the various samples after the thermal treatment at 600 °C have been reported in Table III. From this table a profile shift of 50 nm (at 10¹⁹ at cm⁻³) is deduced for specimen 2SbT. In addition, this shift is backward oriented, i.e., toward the specimen surface; this latter phenomenon will be discussed below.

To explain the occurrence of a shift, which is a rather surprising result, we have tried to simulate the experimental profile assuming the usual value of the diffusion coefficient for Sb (D_{Sb}) that can be computed by extrapolating to 600 °C the Fair's formula³

$$D_{\text{Sb}} = D_i^x + D_i^- \left[\frac{n}{n_i} \right]^2 \quad (4)$$

where D_i^x and D_i^- , respectively, are the neutral and ionized intrinsic diffusion coefficients due to the neutral V^x and to the charged V^- vacancies, while n and n_i are the electron and the intrinsic carrier concentration, respectively. For Sb-doped samples investigated in this work, D_{Sb} depends mainly on the factor $(n/n_i)^2$. In fact the maximum Sb concentration in the samples before the thermal treatment is $n = 1.8 \times 10^{21}$ cm⁻³, while $n_i = 3.54 \times 10^{17}$ cm⁻³ at 600 °C, so that one gets $(n/n_i)^2 = 2.6 \times 10^7$ and $D_{\text{Sb}} = 6 \times 10^{-17}$ cm²/s.

This value introduced in the simulation of the carrier concentration profile after thermal annealing leads to a precipitation Sb fraction consistent with the one determined experimentally. However, it is two orders of magnitude lower than that required to explain the experimental shift in the concentration profile. Moreover, electrical measurements performed on the coimplanted samples gave scattered results, due to the strong compensation, yet with a positive Hall factor, which indicates a prevalence of holes over electrons; as such, the Fermi level is below the band-gap center. Nevertheless, these samples exhibit more or less the same value of the diffusion coefficient, thus indicating that the position of the Fermi level is not the reason for the huge diffusivity observed.

This conclusion is further supported by the fact that in the simulations of 2SbBT, i.e., the only sample where the diffusion shift after thermal annealing is forward, i.e., normal, the shape of the experimental tail (Fig. 2) suggests that the diffusivity is concentration independent; in fact an increased ionized diffusion coefficient D_i^- is not able to reproduce it. Conversely, increasing the neutral intrinsic diffusion coefficient D_i^x by seven orders of magnitude reproduces the shape of the experimental concentration profiles. The reason for this anomalous behavior can be the large amount of vacancies incorporated into the crystal lattice after laser annealing, and demonstrated by our strain measurements. In fact the diffusion activation energy is in large part determined by the vacancy

formation energies, which are 2.6 eV for V^x (Ref. 29) and 3.38 eV for V^- .³⁰ As a consequence, in our experimental conditions the activation energy should be strongly reduced (about 1.2 eV), leading to the seven orders of magnitude increase of the diffusivity. Moreover, in a strongly compensated sample only the state of charge of V^x is stable, the energy level of the charge state of V^- being higher than V^x , meaning that the main fraction of the vacancies are of the V^x type. This fact is confirmed by our EXAFS results after laser annealing, indicating that the vacancies do not form complexes with Sb where they take a charged state but, on the contrary, must form complexes only with Si in the neutral state of charge, the other possible complex B- V being energetically unfavorable. The presence of a large fraction of V^x can influence only D_i^x , explaining the concentration independence of the diffusion.

As far as other thermal-annealed samples are concerned, the most surprising effect is the backward diffusion (i.e., against the concentration gradient). From a comparison between tail diffusion and defect type and density, it comes out that the presence of interfaces (e.g., the precipitate surfaces) as well as of extended defects close to the tail of the concentration profile are the origin of the backward diffusion. For instance, in sample 2SbT, where a high density of defects and 10% of Sb precipitates have been found, the profile shifts backwards by 50 nm, whereas in the defect-free sample 2SbBT the diffusion is normal (i.e., onwards) by 50 nm for Sb and 40 nm for B. Therefore, the observed backward diffusion is a net effect of two phenomena (a usual thermal and an anomalous one) which move the atoms in opposite directions along the depth of the specimen. At the higher dose, the Sb backward diffusion is the same 30–40 nm at 10¹⁹ cm⁻³ both for 5SbT and 5SbBT samples. This indicates that (i) boron does not influence the anomalous Sb diffusivity, and (ii) Sb diffuses not only towards the precipitates, whose fraction decreases from 50 to 10%, but also through the complexes, whose density increases by adding boron. The backward diffusivity of boron is still larger in the 5SbBT sample (–45 nm); this suggests that B diffuses in connection with SbBV complexes.

Another phenomenon which has been observed in this work, and confirms the previous discussion, is the significant outdiffusion of both Sb and B after thermal annealing (Table III). Again, it cannot be explained without assuming the strongly enhanced diffusivity of the dopant at 600 °C. The outdiffused fraction of Sb moderately increases (from 7% to 9%) by increasing the Sb dose, and is strongly related to the crystal defects. In fact, in sample 2SbBT, where no defect is present, there is no outdiffusion of the two dopants; on the other hand, twins and threading dislocations seem to affect more strongly the outdiffusivity of boron than of Sb. This is evident in sample 5SbBT (the defects remaining after the laser treatment are visible in Fig. 8), where the outdiffusion is 19% for boron and 9% for Sb. From these data it is impossible to determine the behavior of the B outdiffusion with dose and defect density, but it seems to be larger than the one of antimony.

In overall, the experimental results indicate that the

position of the Fermi level appears to affect the movement of the atoms around a precipitation site, thus resulting in lower Sb precipitation in coimplanted samples, but not a long-range diffusion. Conversely, the very high carrier concentration present after laser annealing and the inclusion of a high density of vacancies produces strong internal stresses inducing the structure to react, on one side, with extended defects, and, on the other, with a distorted lattice matrix where the dopants have a high probability to join in complexes. These two facts guarantee a huge increase of the dopant mobility during a heat treatment at temperatures as low as 600 °C, giving rise to all the observed phenomena, i.e., precipitation, outdiffusion, and backward diffusion.

V. CONCLUSIONS

In this work it has been demonstrated that when high doses of antimony (2 or $5 \times 10^{16} \text{ cm}^{-2}$) are implanted into silicon and then pulsed laser annealed, thus achieving a very high electron concentration in the heavily doped region, the Sb diffusivity is much larger than expected even for thermal treatments in furnace at temperatures as low as 600 °C. This also occurs in the case of silicon wafers codiffused with the same doses of Sb and B, and thermally processed in the same way. In this case, after laser annealing, a strongly compensated silicon is obtained in the heavily doped zone. Moreover, in some cases antimony and boron outdiffuse from the surface and, still more surprisingly, backdiffuse toward the surface in the tail region of the concentration profile. This behavior is strongly related to the amount and type of crystal defects induced by the different thermal processes. From the ex-

perimental results the following conclusions can be drawn.

(i) The increased Sb diffusivity cannot be explained on the basis of a variation of the Fermi-level position, but by a huge increase, by seven orders of magnitude, in the concentration-independent preexponential D_0 term in the equation of the diffusion coefficient. This is due to the lattice defects, including the high concentration of vacancies which must be generated by laser annealing, as indicated by the strain measurements.

(ii) The dopant outdiffusion is favored by the incomplete regrowth of the silicon lattice after laser annealing, even for the lower dose. Dislocations and twins seem to provide a preferential path for this phenomenon.

(iii) The backward diffusion (i.e., against the concentration gradient) occurs whenever lattice defects are present in the region of the profile's tail. Sb precipitates seems to be most effective as a sink for this anomalous diffusion. In the case where no extended defect is detected, the dopants diffuse inwards, as expected.

(iv) In the codiffused samples, antimony and boron diffuse together, which is in part related to the formation of Sb-B pairs, previously reported in literature and detected by EXAFS in our samples, particularly for the higher implantation dose.

ACKNOWLEDGMENTS

The authors are indebted to S. Solmi for many stimulating discussions and for critically revising the text. The technical assistance of F. Corticelli, A. Garulli, and D. Govoni is also gratefully acknowledged.

¹Th. Wicher, M. L. Swanson, and A. F. Quenville, *Phys. Rev. Lett.* **57**, 1759 (1986).

²R. J. Culbertson and S. J. Pennycook, in *Beam-Solid Interactions and Transient Processes*, edited by M. O. Thompson, S. T. Picraux, and J. S. Williams, MRS Symposia Proceedings No. 74 (Materials Research Society, Pittsburgh, 1987), p. 391.

³R. B. Fair, M. L. Manda, and J. J. Wortman, *J. Mater. Res.* **1**, 705 (1986).

⁴N. E. B. Cowern, *Appl. Phys. Lett.* **54**, 703 (1989).

⁵B. Margesin, R. Canteri, S. Solmi, A. Armigliato, and F. Baruffaldi, *J. Mater. Res.* **6**, 2353 (1991).

⁶P. E. Andersen, A. Nylandsted-Larsen, P. Tidemand-Petersson, and G. Weyer, *J. Appl. Phys.* **71**, 755 (1988).

⁷J. L. Allain, A. Bourret, J. R. Regnard, and A. Armigliato, *Appl. Phys. Lett.* **61**, 264 (1992).

⁸J. W. Mayer and E. Rimini, *Ion Beam Handbook for Material Analysis* (Academic, New York, 1977).

⁹J. U. Andersen, E. Laegsgaard, and L. C. Feldman, *Radiat. Eff.* **12**, 219 (1972).

¹⁰C. Cohen, J. A. Davis, A. V. Drigo, and T. E. Jackman, *Nucl. Instrum. Methods Phys. Res.* **218**, 147 (1983).

¹¹A. Armigliato, G. G. Bentini, G. Ruffini, G. Battaglin, G. Dalla Mea, and A. V. Drigo, *Nucl. Instrum. Methods* **149**, 653 (1978).

¹²A. Carnera and A. V. Drigo, *Nucl. Instrum. Methods Phys.*

Res. Sect. B **44**, 357 (1990).

¹³T. J. Van Netten, K. Stapel, and L. Niesen, *J. Phys. (Paris) Colloq.* **8**, C-1049 (1986).

¹⁴R. W. G. Wyckoff, *Crystal Structures* (Krieger, Huntington, NY, 1982).

¹⁵F. Bechstedt and W. A. Harrison, *Phys. Rev. B* **39**, 5041 (1989).

¹⁶S. J. Gurman, N. Binsted, and I. Ross, *J. Phys. C* **17**, 143 (1984).

¹⁷A. Garulli, A. Armigliato, and M. Vanzi, *J. Microsc. Spectrosc. Electron.* **10**, 135 (1985).

¹⁸J. Narayan and J. Fletcher, in *Defects in Semiconductors*, edited by J. Narayan and T. Y. Tan, MRS Symposia Proceedings No. 2 (Materials Research Society, Pittsburgh, 1981), p. 191.

¹⁹A. Parisini and A. Bourret, *Phys. Mag.* **67**, 605 (1993).

²⁰L. C. Feldman, J. W. Mayer, and S. T. Picraux, *Materials Analysis by Ion Channeling* (Academic, New York, 1982).

²¹J. Lindhard, *K. Dan. Vidensk. Selsk. Mat. Fys. Medd.* **34**, No. 1 (1965).

²²D. Nobili, *Properties of Silicon*, EMIS Datareviews Series No. 4 (INSPEC, London, 1988), p. 401.

²³D. Nobili, *Properties of Silicon* (Ref. 22), p. 384.

²⁴L. Pauling, *The Nature of the Chemical Bond* (Cornell University Press, Ithaca, NY, 1960), p. 246.

²⁵G. Celotti, D. Nobili, and P. Ostoja, *J. Mater. Sci.* **9**, 821

- (1974).
- ²⁶A. Nylandsted-Larsen, F. T. Pedersen, G. Weyer, R. Galloni, R. Rizzoli, and A. Armigliato, *J. Appl. Phys.* **59**, 1908 (1986).
- ²⁷R. J. Culbertson and S. J. Pennycook, in *Beam-Solid Interactions and Transient Processes* (Ref. 2), p. 391.
- ²⁸S. Solmi, F. Baruffaldi, and M. Derdour, *J. Appl. Phys.* **71**, 697 (1992).
- ²⁹R. P. Messmer, in *Lattice Defect in Semiconductors, 1974* (The Institute of Physics and Physical Society, Bristol, 1975), p. 44.
- ³⁰R. B. Fair, in *Impurity Doping Processes in Silicon*, edited by F. F. Y. Wang (North-Holland, Amsterdam, 1981), pp. 317–442.

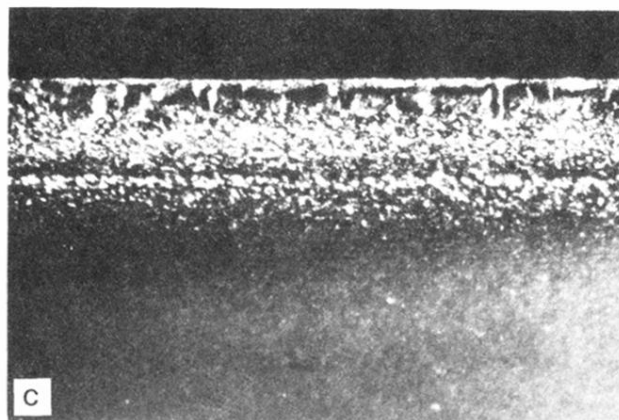
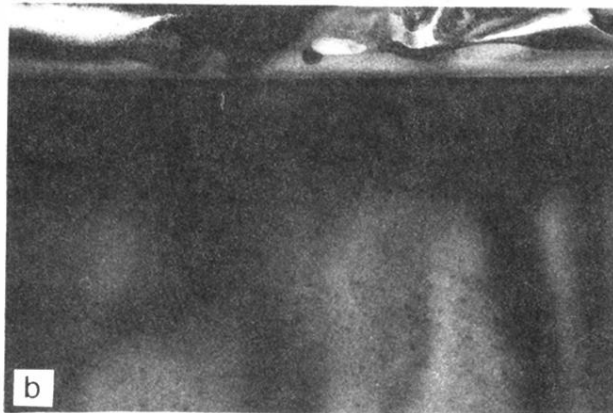
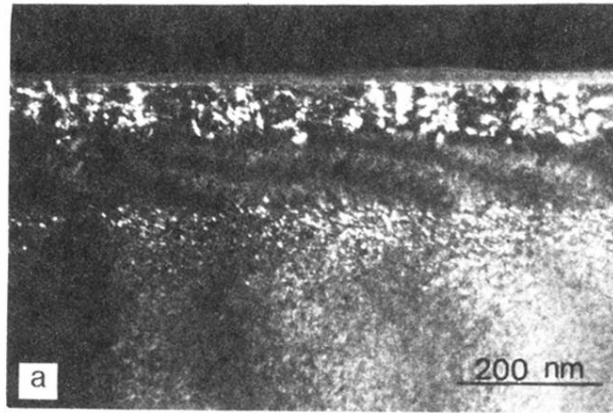


FIG. 3. TEM micrographs taken in the lower-dose samples (a) 2SbL, WBDF; (b) 2SbBL, BF, (c) 2SbT, WBDF.

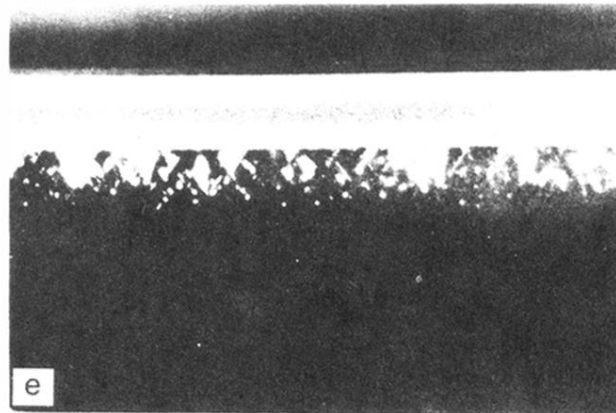
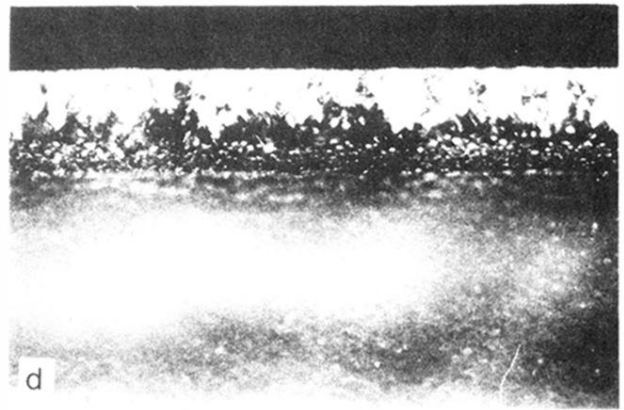
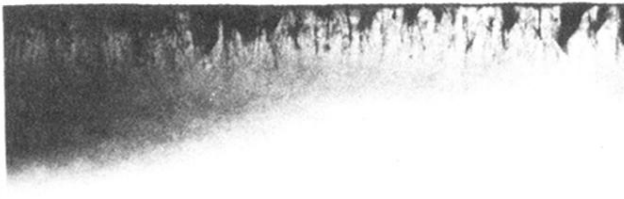
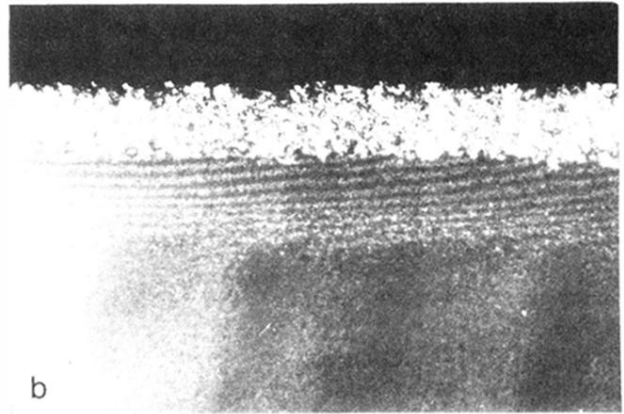
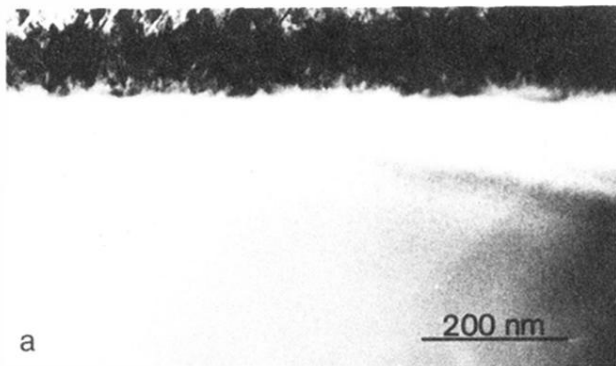


FIG. 8. TEM images taken on the higher-dose samples. (a) 5SbL, BF; (b) 5SbL, WBDF; (c) 5SbBL, BF; (d) 5SbT, DF; and (e) 5SbBT, DF. The last two micrographs have been obtained by including spots from the twins and the Sb precipitates in the objective aperture.